



Research Paper

Highly efficient g-C₃N₄/TiO₂/kaolinite composite with novel three-dimensional structure and enhanced visible light responding ability towards ciprofloxacin and *S. aureus*



Chunquan Li, Zhiming Sun*, Wanzhong Zhang, Caihong Yu, Shuilin Zheng*

School of Chemical and Environmental Engineering, China University of Mining and Technology (Beijing), Beijing 100083, PR China

ARTICLE INFO

Keywords:

g-C₃N₄
TiO₂
Kaolinite
Visible light
Ciprofloxacin
S. aureus

ABSTRACT

A novel 3D heterogeneous g-C₃N₄/TiO₂/kaolinite composite with enhanced visible light activity was fabricated via a mild sol-gel method associated with chemical stripping and self-assembly. Compared with bare photocatalysts, the g-C₃N₄/TiO₂/kaolinite 3D structure exhibits enhanced adsorption-photocatalytic degradation ability for the removal of ciprofloxacin (CIP) under visible-light irradiation, and also facilitate the recyclability of the photocatalyst as demonstrated from the reusability test. The apparent rate constant of the composite is up to around 5.35 times, 6.35 times and 4.49 times that of bare TiO₂, g-C₃N₄ and P25, respectively, and a possible degradation pathway was also proposed. On the other hand, the as-received composite also exhibited enriched disinfection ability towards *S. aureus*. It is indicated that the superoxide radical ($\cdot\text{O}_2^-$) is the main active species in the degradation process, and the superior photocatalytic performance of composite should be mainly attributed to both the improvement of light harvesting as well as the enhanced separation and transfer efficiency. It is expected that this novel ternary visible-light responding composite would be a promising candidate material for the organic pollutants degradation and bacteria inactivation.

1. Introduction

With the rapid development of human beings' industry and civilization, water pollution is gradually becoming more and more serious. Currently, both water-contained antibiotic and waterborne bacteria are regarded as the major groups of water contaminants due to their ubiquitous property and hazardous biological and ecotoxicological effects [1,2]. Pharmaceuticals and personal care products (PPCPs) like ciprofloxacin are usually derived from industries, hospitals and domestic sites effluents. Sometimes, they are directly thrown into the surface and ground waters without any previous decontamination treatment, resulting in pollution and disturbing effects. Besides, this kind of pollutant cannot be completely removed or transformed through conventional wastewater treatment methods like adsorption, membrane filtration and chemical oxidation [3,4]. Therefore, high-efficient removal and degradation of these pharmaceuticals has become a hot topic of environmental scientific research in recent years. On the other hand, waterborne bacteria (*S. aureus*) may pose significant health risks to human as well, which are generally difficult to be fully inactivated due to their small size and high resistance to harsh environmental conditions. Hence, efficient removal of bacteria is also urgently needed to

guarantee the safety of drinking water [5]. In recent years, advanced oxidation processes (AOPs) especially for photocatalysis are well-accepted technologies to be used in the field of persistent organic pollutants degradation as well as bacteria inactivation [6,7]. Photocatalysis technique has been considered to be a desired strategy for environmental remediation because of its low-cost, environmental benefit, nontoxicity and stability [8].

However, conventional semiconductor catalysts like TiO₂ and g-C₃N₄ usually have a poor activity, narrow spectral response and limited electron transportation, which severely restricted their practical application. Hence, more and more effort has been focused on exploring the high-efficiency visible-light photocatalysts in recent decades [9]. According to previous reports [10,11], heterojunctions like g-C₃N₄/TiO₂ usually exhibit superior photoactivity than single photocatalyst through constructing two photo-reactive semiconductors with suitable electronic structures. The accelerated charge separation by the internal electric field in the heterojunctions is the main driving force of photocatalytic performance enhancement [12]. On the other hand, it is widely accepted that natural minerals is a good choice as the catalyst carriers to construct the macro-micro system considering their high adsorption ability, thermal and chemical stability, low cost, easy

* Corresponding authors.

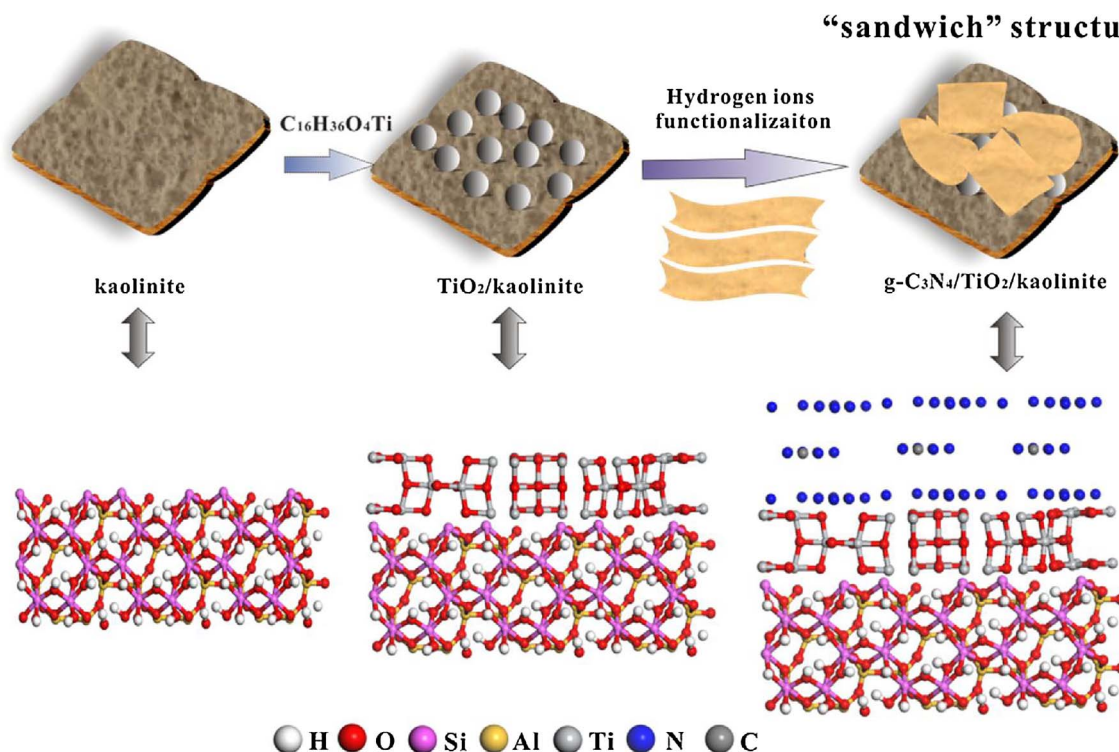
E-mail addresses: zhimingsun@cumbt.edu.cn (Z. Sun), shuilinzheng8@gmail.com (S. Zheng).

<http://dx.doi.org/10.1016/j.apcatb.2017.08.044>

Received 1 May 2017; Received in revised form 5 July 2017; Accepted 14 August 2017

Available online 19 August 2017

0926-3373/ © 2017 Elsevier B.V. All rights reserved.



Scheme 1. Schematic illustration of synthesis strategy for g-C₃N₄/TiO₂/kaolinite composite.

recycling and abundance [13–15]. In the past decades, the composites based on the combination between natural minerals and TiO₂ or g-C₃N₄ has been widely studied. However, most of such composites like TiO₂/montmorillonite or g-C₃N₄/montmorillonite are just responding to ultraviolet or limited visible light [16–19]. Hence, it is meaningful and feasible to synthesize a ternary photocatalyst through the combination between g-C₃N₄/TiO₂ heterojunction and natural minerals in order to construct a highly efficient adsorption and visible-light-driven photocatalytic degradation system.

In our present work, a kind of novel ternary g-C₃N₄/TiO₂/kaolinite composite with a “sandwich” structure was first designed and constructed, which would be beneficial for the utilization of solar energy as well as regulating the path and velocity of the generated electron-hole pairs [20]. Ciprofloxacin (CIP) and *S. aureus* were taken as the target degradation pollutants in this study. A possible mechanism for the enhanced and stable photoactivity was also investigated and proposed based on the characterization results.

2. Experimental

2.1. Materials

The purified kaolinite was obtained from Suzhou City, Jiangsu Province. Tetrabutyl titanate (C₁₆H₃₆O₄Ti, TBOT) was bought from Maya Reagent Co. (Zhejiang, China). Ciprofloxacin was purchased from Aladdin Industrial Corporation. Dicyandiamide was gained from Tianjin Jinke Fine Chemical Research Institute. Hydrochloric acid (HCl) and sulphuric acid (H₂SO₄) were purchased from Sinopharm Chemical Reagent Co., Ltd (Beijing, China). HPLC-grade formic acid, methanol and acetonitrile were achieved from Merck Co. Degussa P25 (Dusseldorf, Germany) consists of 75% anatase and 25% rutile with a specific BET surface area of ca. 50 m²/g was used as a reference in this work. Beijing Reagent Co. (Beijing, China) provided the ethanol (C₂H₅OH), acetic acid (CH₃COOH), isopropanol (IPA), 1, 4-benzoquinone (BQ), edentate disodium (EDTA-2Na) and other chemicals used in our experiments. All of them were analytical reagent grade. Deionized

water was used throughout all our experimental procedures.

2.2. Catalyst preparation

The fabrication procedures of g-C₃N₄ powders was the same as our previous reports [21]. Typically, 15 g of dicyandiamide was added into an alumina crucible with a cover, and then heated to 550 °C for 4 h with a heating rate of 2.3 °C min^{−1}. After cooling to room temperature, the resulted yellow product was collected and ground into powder for further use.

In this study, kaolinite was firstly used as the carrier of TiO₂. The preparation procedures of TiO₂/kaolinite composite as well as TiO₂ were conducted as follows. First, 1.0 g kaolinite was added to a mixture constituted by 24.0 mL of ethanol and 2.0 mL of acetic acid under stirring in the water bath for 30 min at 25 °C. Next, 3 mL of TBOT were put drop-wise into the kaolinite suspensions. After continuous stirring for 30 min, 28.0 mL of ethanol: water solution (v: v = 1:1; pH = 2) was added into the above suspensions drop by drop through a peristaltic pump. The obtained mixture was then stirred continuously for 12 h to immobilize the as-generated TiO₂ colloids on the kaolinite surface. In the following step, the resultant product was dried in an oven at 80 °C for 12 h. Finally, the samples were calcined under 500 °C for 2 h in air with a heating rate of 5 °C/min. The bare TiO₂ was prepared by a similar method as TiO₂/kaolinite composite without adding kaolinite.

The g-C₃N₄/TiO₂/kaolinite composite was synthesized based on the following steps. Firstly, the synthesized TiO₂/kaolinite composite was put into the sulfuric acid solution (5 mol/L, 50 mL). It could be calculated that the theoretical content of TiO₂ in the TiO₂/kaolinite composite is around 41.35%. In the second step, 0.295 g as-prepared g-C₃N₄ powders were added into the above solution and stirred continuously for 24 h at 25 °C. Then, the resulted product was centrifugated and filtrated to neutral. After dried at 60 °C for 12 h, the achieved composite was simple grinded and collected. The theoretical load content of heterogeneous g-C₃N₄/TiO₂ in the final obtained g-C₃N₄/TiO₂/kaolinite composite is 50.0% in this work. The probable synthesis strategy for g-C₃N₄/TiO₂/kaolinite composite was illustrated in Scheme 1.

Furthermore, g-C₃N₄/kaolinite and g-C₃N₄/TiO₂ composites were also prepared based on the above-mentioned procedures. The g-C₃N₄/kaolinite was prepared through adding 1 g of kaolinite and 1 g of g-C₃N₄ into the sulfuric acid solution (5 mol/L, 50 mL), then centrifugated and filtrated to neutral after stirring for 24 h at 25 °C. As for the g-C₃N₄/TiO₂ composite, 0.6 g of g-C₃N₄ and 1.4 g of TiO₂ was also put into 50 mL sulfuric acid with a solution concentration of 5 mol/L. After stirring for 24 h at 25 °C, the prepared composite was centrifugated and filtrated to neutral as well.

2.3. Characterizations

X-ray diffraction patterns were recorded on a D8 advance X-ray diffractometer (Bruker, Germany) by using Cu-K α radiation ($\lambda = 0.154056$ nm). The range of 2θ was from 10° to 80° with a 0.02° step at a scanning speed of 4°/min. SEM images, EDS patterns and element mapping images were recorded on an S-4800 scanning electron microscopy (Hitachi, Japan) equipped with an energy dispersive spectroscope at 5.0 kV. Besides, TEM and HRTEM images were collected on the Tecnai G2 F20 Field Emission Transmission Electron Microscope and JEM-3010 Electron Microscope, operating at 200 kV. Room temperature UV–vis absorption spectroscopy was conducted on a Hitachi U-3010 spectrophotometer using an integrating-sphere accessory. The band gap values of different photocatalysts were estimated by extrapolating the linear part of the plot of $(F(R)h\nu)^{1/2}$ versus $h\nu$: $F(R)h\nu = A(h\nu - E_g)^2$, where $F(R) = (1-R)^2/2R$ stands for the Kubelka–Munk function calculated from the reflectance spectrum and $h\nu$ is the photon energy expressed in eV. The Brunauer–Emmett–Teller (BET) specific surface area of samples was determined at liquid nitrogen temperature (77 K) on a JW-BK (JWGB Sci. & Tech, Beijing) nitrogen adsorption apparatus. Pore-size distributions were calculated from the adsorption branch of the isotherm, according to the Barrett–Joyner–Halenda (BJH) model. PL spectra of the catalysts were measured on the F-7000 spectrometer (Hitachi, Japan) with an excitation wavelength of 400 nm for g-C₃N₄ and g-C₃N₄/TiO₂/kaolinite composite as well as 300 nm for TiO₂. The photocurrent and electrochemical impedance spectroscopy (EIS) were measured with an electrochemical analyzer (CHI-660B, China).

2.4. Photoactivity measurements

The photocatalytic activities of as-prepared g-C₃N₄/TiO₂/kaolinite composite as well as the comparative samples were evaluated by the degradation of ciprofloxacin (CIP) under a Xenon lamp (average light intensity 90 mW/cm², PL-03, Beijing Pulinsaisi plant, China) with a 400 nm cut-off filter. In a typical experiment, 0.2 g of the as-prepared catalysts was dispersed in 100 mL of standard CIP (10 ppm) aqueous solution and underwent ultrasonic treatment for 10 min to form stabilized suspension. The suspension was then added into the cylindrical reactor under constant magnetically stirring. 1 h dark reaction was conducted to achieve the adsorption-desorption equilibrium on the surface of composites. In the specific time interval, 2 mL of suspension was sampled and separated through centrifugation at 8000 rpm for 5 min. Photodegradation effect was evaluated by measuring the absorbance of the solution at 278 nm (CIP) on a UV–vis spectrophotometer (UV-9000s, Shanghai Metash). Comparative experiments were carried out under the same conditions using pure g-C₃N₄, kaolinite, TiO₂, TiO₂/kaolinite, g-C₃N₄/kaolinite, g-C₃N₄/TiO₂ and Degussa P25 as references. All the removal data of batch experiments were obtained in parallel.

2.5. Analysis of degradation products of CIP

The intermediates analysis was performed by a LC/MS system (Agilent 1200 series, Ion Trap) equipped with a Welch Ultimate XB-C18 column (250 mm \times 4.6 mm i.d., 5 μ m). The mobile phase was

composed of water (A) and acetonitrile (B) containing 0.1% formic acid (v/v) and the flow rate was 1.0 mL/min. The gradient started with 15% B, increased to 35% within 25 min, to 95% within 35 min, then returned to initial composition within 10 min and equilibrated within 10 min. The injection volume was 10 μ L and the column temperature was 30 °C. MS was performed by operating in the positive ion mode using ESI under the following conditions: capillary, 25 nA; nebulization pressure, 35 psi; temperature of drying gas, 350 °C; drying gas flow, 10 L/min. MS was scanned by mass range from m/z 50–800 [6].

2.6. Bacterial culture and antibacterial experiments

In this study, *Staphylococcus aureus* (*S. aureus*) was multiplied at 37 °C based on the Nutrient Broth (NB) medium. After an approximately 12 h germiculture, the bacterial concentration could be detected as around 1×10^8 cfu/mL. Then the cultured bacteria were centrifugated at 5000 rpm for 10 min, the supernatant was removed and the resultant bacterial precipitation was shaken and suspended in sterile physiological water (NaCl, 0.85%) to obtain an initial bacterial concentration of around 1×10^7 cfu/mL.

The photocatalytic tests were assessed using an experimental apparatus as follow. A quartz tube (100 mL) was used as a single liquid-phase photocatalytic reactor to determine the antibacterial ability of different materials towards *S. aureus*. In each experiment, different samples were added into the reactors with a concentration of 30 mg/L. After the addition of the bacteria, dark reaction (1 h) and visible light irradiation (5 h) were conducted in sequence. The mixtures were agitated with a magnetic stirrer (170r/min) to ensure adequate mixing and contact between catalysts and bacteria. The light source was an 8 W fluorescent lamp (Philips) and the vertical distance between the lamp and the reactors is around 20 cm. At each time interval, the bacterial suspension was sampled and diluted in sterile physiological water. Finally, 100 μ L of the resulted bacterial solutions were spread on the Nutrient Agar. Each agar plate was incubated at 37 °C and 65% RH for 24 h, and then the bacteria were counted with an electronic counter. All the experiments were performed in triplicate. The efficiency of photocatalysis was reported as $\log(C_t/C_0)$, where C_0 and C_t were the concentration of survival bacteria before and after inactivation, respectively. All materials used in the experiments contacting bacteria were sterilized by autoclaving at 121 °C for 30 min.

2.7. Photoelectrochemical measurement

To investigate the photoelectrochemical properties of the as-prepared samples, the working electrodes were prepared similar to our previous report: 10 mg of the as prepared photocatalysts were suspended in 1 mL ethanol and ultrasonicated for 15 min to generate the slurry. Then, the resulting suspensions were dropped onto the ITO slices with a fixed area of 2 cm² and dried in air. Finally, they were transferred to the oven for 4 h at 80 °C. All the photoelectrochemical measurements were conducted on an electrochemical analyzer in a standard three-electrode system using the prepared samples as the working electrodes, a Pt wire as the counter electrode, and Ag/AgCl as a reference electrode. A 500 W Xe arc lamp served as the light source. The photocurrent and electrochemical impedance spectroscopy (EIS) was performed in 0.1 M Na₂SO₄ aqueous solution [22].

3. Results and discussion

The general morphologies and microstructures of kaolinite, TiO₂/kaolinite, TiO₂, g-C₃N₄ and g-C₃N₄/TiO₂/kaolinite were investigated by SEM analysis (Fig. 1(a–e)). It is indicated that kaolinite exhibited layered structures composed of many parallel nanosheets with 0.3–1 μ m in width and 10–20 nm in thickness. The kaolinite has a smooth and regular surface without impurities, which could significantly promote the assembly of nano TiO₂ particles. From Fig. 1(b),

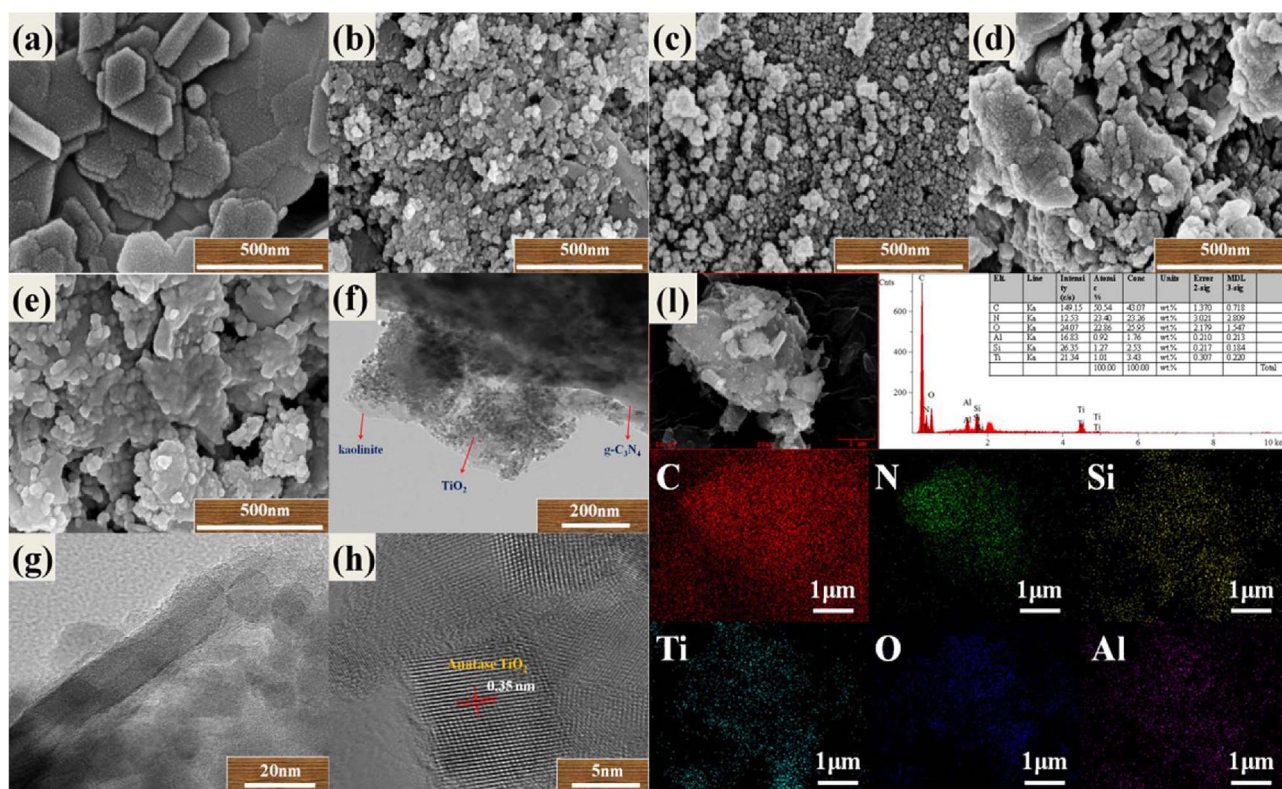


Fig. 1. FESEM images of (a) kaolinite, (b) TiO₂/kaolinite, (c) TiO₂, (d) g-C₃N₄, (e) g-C₃N₄/TiO₂/kaolinite composite, HRTEM images of (f, g and h) g-C₃N₄/TiO₂/kaolinite composite, and (i) EDS spectrum as well as element mapping of C, N, Ti, O, Si and Al for g-C₃N₄/TiO₂/kaolinite composite, the upper left corner shows the corresponding images.

it is indicated that the TiO₂/kaolinite well solved the agglomeration and high surface energy of pure TiO₂ (Fig. 1(c)). As for the pure g-C₃N₄, bulk morphology with wrinkled structure was formed due to the 2D nanosheets aggregated and stacked with each other in the process of thermal polymerization. The morphology of g-C₃N₄/kaolinite composite prepared in this work was also presented in Fig. S4. 2D/2D structure was obtained due to the layered character of the compositions. As for the g-C₃N₄/TiO₂/kaolinite composite (Fig. 1(e)), 3D “sandwich” structure was successfully established through the hydrogen ions functionalized process. Tight combination and highly exposed edges were obtained through this assembly as well, which significantly increased the number of active sites and would be beneficial for the transfer and migration of generated carriers [23]. It is clear that the g-C₃N₄/TiO₂/kaolinite composite has a looser porous structure compared with the above-mentioned single materials.

High-resolution transmission electron microscope (HRTEM) was adopted to further explore the structural insights of the synthesized g-C₃N₄/TiO₂/kaolinite composite. As shown in Fig. 1(f and g), dense and uniform nano particles were decorated on the surface of kaolinite, and unique “sandwich” structure was formed after the introduction of g-C₃N₄. This is in good agreement with the SEM observations. Some other SEM and TEM images were also provided in Fig. S1 and S2, which could further demonstrate the formation of the heterogeneous “sandwich” structure. The obvious morphological difference indicated the important role of kaolinite as an outstanding and stable substrate for the nucleation and growth of g-C₃N₄/TiO₂ heterojunction. Furthermore, the lattice fringe images of g-C₃N₄, TiO₂ and kaolinite in the g-C₃N₄/TiO₂/kaolinite composite were presented in Fig. 1(h) and Fig. S3. These images not only clearly revealed the well-stacked sphere-like structure of anatase TiO₂ with a lattice of 0.35 nm, but also exhibited the (002) and (200) crystal surface of kaolinite, which corresponded to the crystal spacing of 0.36 nm and 0.25 nm, respectively. However, the lattice fringes of g-C₃N₄ and kaolinite are indistinct compared with TiO₂, this could attributed to the weak crystalline of g-C₃N₄ and poor

thermostability of kaolinite. Energy dispersive spectrometer (EDS) and element mapping was used to identify the elemental compositions of the as-prepared g-C₃N₄/TiO₂/kaolinite composite as well. It is indicated that the “sandwich” structure is mainly composed with C, N, Ti, O, Si and Al. All of these elements are relatively homogeneous distributions within the composite, which further demonstrated the well distribution of g-C₃N₄/TiO₂ heterojunction on the surface of natural layered kaolinite.

The crystallographic structures of kaolinite, TiO₂/kaolinite, TiO₂, g-C₃N₄ and g-C₃N₄/TiO₂/kaolinite were analyzed by X-ray diffraction (XRD) measurement (Fig. 2(a)). The XRD pattern of kaolinite clearly displayed (001) diffraction peak of kaolinite at 12.28°, indicating the d spacing of 0.72 nm as calculated by Bragg’s equation, which was well corresponded to the standard pattern (JCPDS No.14-0164). Other several peaks at 24.82°, 38.34° and 62.26° were well matched to the (002), (-202) and (060) lattice planes of triclinic kaolinite as well. The characteristic peaks of kaolinite disappeared as exhibited in the as-synthesized TiO₂/kaolinite and g-C₃N₄/TiO₂/kaolinite, which might be attributed the loss of the stacking between the kaolinite layers during the calcination as well as the completion of the dehydroxylation reaction [18]. The bare g-C₃N₄ shows the highly crystalline (JCPDS No.87-1526) and two characteristic peaks at 12.74° and 27.60° was observed. The characteristic peaks of TiO₂ at 25.36°, 37.84°, 48.12°, 53.96°, 55.16° and 62.76° corresponded to the (101), (004), (200), (105), (211) and (204) crystal planes of anatase TiO₂ (JCPDS 21-1272) appears in the as-prepared TiO₂, TiO₂/kaolinite, and g-C₃N₄/TiO₂/kaolinite composite [11]. Besides, the (101) diffraction peak of TiO₂ and the (002) diffraction peak of g-C₃N₄ in the g-C₃N₄/TiO₂/kaolinite composite possessed slight shift compared with the comparative samples (Fig. 2(b)), indicating the generation of lattice distortion in the g-C₃N₄/TiO₂/kaolinite composite and a successful construction of the ternary heterogeneous system. According to the Debye-Scherrer equation, the average crystalline sizes of pure TiO₂, TiO₂/kaolinite and g-C₃N₄/TiO₂/kaolinite composite were calculated and listed in Table 1. The grain sizes of

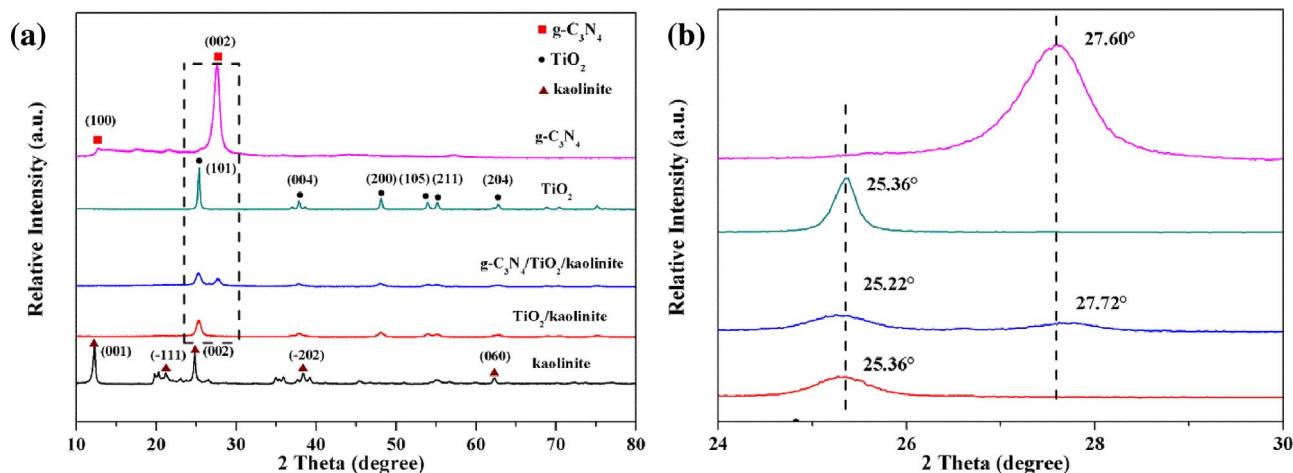


Fig. 2. (a) XRD patterns for kaolinite, $\text{TiO}_2/\text{kaolinite}$, TiO_2 , $\text{g-C}_3\text{N}_4$ and the as-prepared $\text{g-C}_3\text{N}_4/\text{TiO}_2/\text{kaolinite}$ composite, (b) the corresponding enlarged area marked with dashed lines in Fig. 2(a).

Table 1

Surface and structural characterization of $\text{g-C}_3\text{N}_4/\text{TiO}_2/\text{kaolinite}$ composite as well as the comparative samples.

Sample	S_{BET} (m^2/g)	Pore Volume (cm^3/g)	Average pore radius (nm)	Crystallite size of TiO_2 (nm)
kaolinite	22.507	0.048	8.587	–
TiO_2	28.946	0.079	10.943	30.40
$\text{g-C}_3\text{N}_4$	24.901	0.051	8.151	–
$\text{g-C}_3\text{N}_4/\text{TiO}_2/\text{kaolinite}$	51.596	0.100	7.768	14.21

TiO_2 were decreased significantly from around 30 nm to 14 nm after the introduction of kaolinite. It is indicated that the introduction of kaolinite could effectively control the grain size of the loaded TiO_2 nanoparticles, which would be beneficial for the enhancement of photoactivity.

Fig. 3 shows the UV–vis diffuse reflectance spectra (DRS) of the as-prepared samples. As shown in Fig. 3(a), the kaolinite displayed lower light absorption ability within the full wavelength range, which might be attributed to the light scattering effect derived from compositions and structures of natural minerals. Besides, the pure TiO_2 exhibits an absorption edge at around 405 nm, corresponding to the electronic transition from O^{2-} anti-bonding orbital to the lowest empty orbital of Ti^{4+} ($\text{O}2\text{p} \rightarrow \text{Ti}3\text{d}$) [24]. As for the newly prepared $\text{g-C}_3\text{N}_4/\text{TiO}_2/\text{kaolinite}$ composite, it is noticed that the optical absorption edge extended

to around 455 nm. Red shift was generated compared with the comparative samples (TiO_2 and $\text{TiO}_2/\text{kaolinite}$), which would contribute to the absorption of visible light. In addition, in comparison with bare $\text{g-C}_3\text{N}_4$, the absorbance intensity of the heterogeneous composite presented a significant enhancement in the visible light region ranging from 450 to 800 nm. This phenomenon demonstrated that the constructed “sandwich” structure may enhance the visible light utilization efficiency, which would be favorable for the photocatalysis. Moreover, the plots obtained via the transformation based on the Kubelka-Munk function versus the photo energy were shown in Fig. 3(b). The optical band gap of the as-achieved samples is estimated by extrapolating the linear region of the Kubelka-Munk function plots to the photon energy axis, which revealed the optical band gap of 3.10 eV, 3.05 eV, 2.72 eV and 2.72 eV for $\text{TiO}_2/\text{kaolinite}$, TiO_2 , $\text{g-C}_3\text{N}_4$ and $\text{g-C}_3\text{N}_4/\text{TiO}_2/\text{kaolinite}$, respectively. The as-synthesized $\text{g-C}_3\text{N}_4/\text{TiO}_2/\text{kaolinite}$ composite possessed the lowest band gap, which implied that the intermediate level was produced and more visible light would be harvested within unit time.

To further understand the role of TiO_2 , $\text{g-C}_3\text{N}_4$ and kaolinite in $\text{g-C}_3\text{N}_4/\text{TiO}_2/\text{kaolinite}$ composite, the surface area and pore structure of $\text{g-C}_3\text{N}_4/\text{TiO}_2/\text{kaolinite}$ composite as well as the comparative samples were investigated by N_2 adsorption-desorption isotherms as shown in Fig. 4. The N_2 adsorption-desorption isotherms curves of TiO_2 and $\text{g-C}_3\text{N}_4/\text{TiO}_2/\text{kaolinite}$ composite exhibited a type IV adsorption branch with a H3 hysteresis loop, which is characteristic of the mesoporous structure. However, the pure kaolinite and $\text{g-C}_3\text{N}_4$ presented a typical II

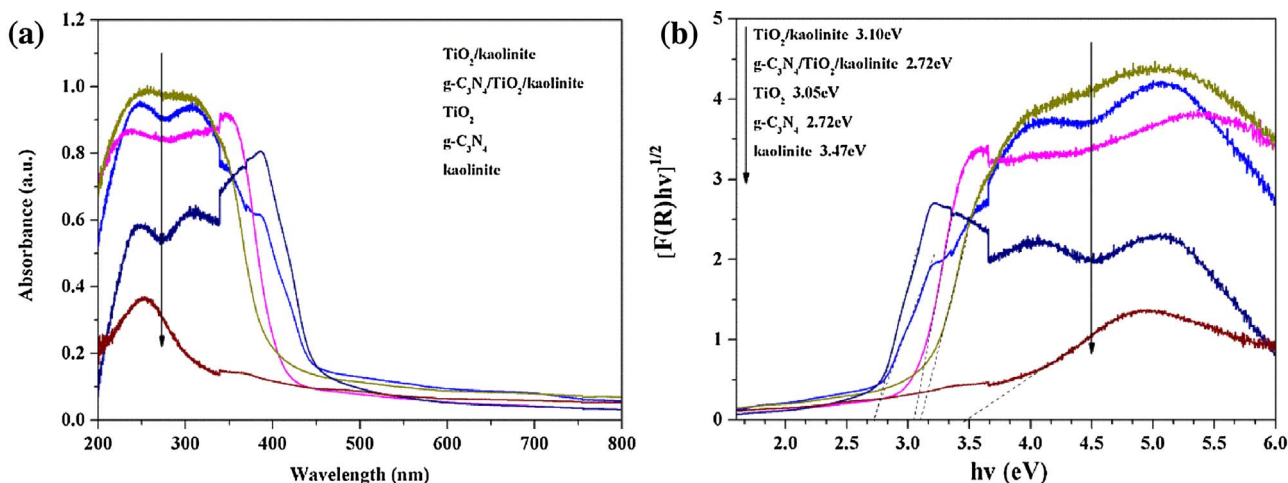


Fig. 3. UV–vis DRS (a) and band gaps (b) of kaolinite, $\text{TiO}_2/\text{kaolinite}$, TiO_2 , $\text{g-C}_3\text{N}_4$ and the as-prepared $\text{g-C}_3\text{N}_4/\text{TiO}_2/\text{kaolinite}$ composite.

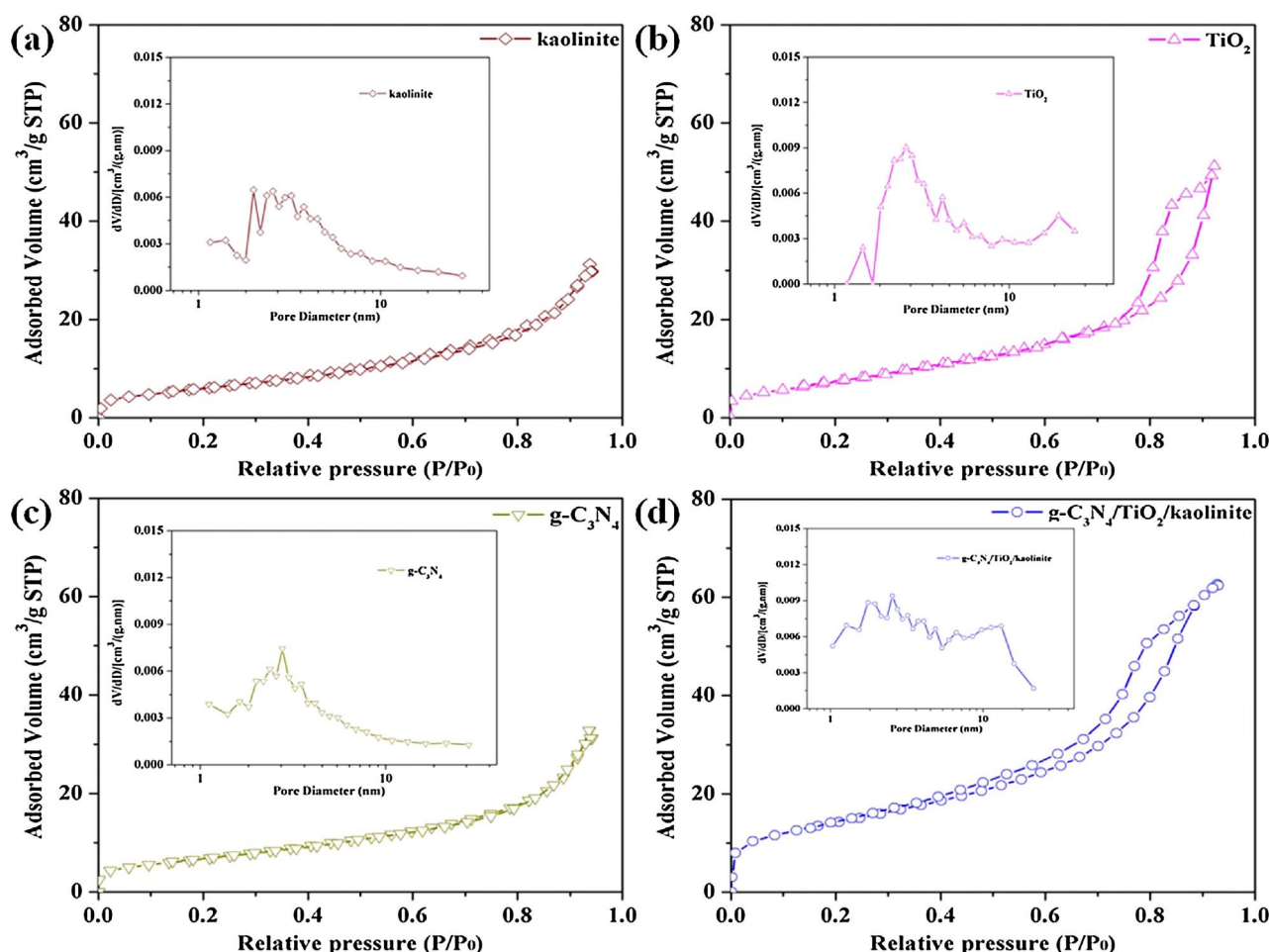


Fig. 4. N₂ adsorption and desorption isotherms measured at 77 K as well as BJH pore size distribution plots of (a) kaolinite, (b) TiO₂, (c) g-C₃N₄ and (d) the as-prepared g-C₃N₄/TiO₂/kaolinite composite.

adsorption branch, which indicated the nonporous and macroporous characters combining with the morphological results. As presented in Table 1, the specific surface area and the total pore volume of g-C₃N₄/TiO₂/kaolinite composite are higher than those of kaolinite, TiO₂ and g-C₃N₄. The large surface area and pore volume of g-C₃N₄/TiO₂/kaolinite composite could be attributed to the uniform distribution of nano TiO₂ particles and the unique construction of “sandwich” structure, which could effectively promote the enhancement of catalytic activity through generating more adsorption and reactive sites. The average pore diameters were also calculated by Barrett-Joyner-Halenda (BJH) method in this study. The g-C₃N₄/TiO₂/kaolinite composite has a wider pore size distribution from 1 nm to 20 nm compared with the other comparison samples. And the least average pore diameter (7.768 nm) was obtained for the g-C₃N₄/TiO₂/kaolinite composite in this work as well, which would be also beneficial for the adsorption, migration and degradation of target contaminations.

The photocatalytic activities of the samples were evaluated by the reduction reaction of ciprofloxacin (CIP) in the aqueous phase under visible light illumination. The progress of reaction can be monitored by measuring the absorbance of the reduction solution. The reduction of CIP is a thermodynamically and kinetically feasible process, thus it can be adopted as a probe in the field of photodegradation. Seen from Fig. 5(a), in the presence of TiO₂, g-C₃N₄ and P25, only about 35% removal rate was obtained after reacting for 4 h, which might be ascribed to the wide band gap of bare photocatalysts. On the other hand, as for g-C₃N₄/TiO₂/kaolinite composite, it is clear that the composite has stronger adsorption ability compared with other comparative samples, including the as-prepared g-C₃N₄/TiO₂, which could be

attributed to the abundant adsorption and reaction sites on the surface of layered kaolinite. All samples had reached to adsorption equilibrium as demonstrated in the dark zone. The final removal rate of g-C₃N₄/TiO₂/kaolinite composite reached to around 92%, which is much higher than other comparative samples. The comparison between the g-C₃N₄/TiO₂/kaolinite composite prepared in this work with partial reported literatures about TiO₂/montmorillonite, g-C₃N₄/montmorillonite and g-C₃N₄/TiO₂ was listed in Table S1 as well. It is obvious that the TiO₂/montmorillonite composite was just corresponding to ultraviolet, which has poor visible-light degradation efficiency. As for the g-C₃N₄/TiO₂ composite, the g-C₃N₄/TiO₂/kaolinite has a much higher ability in degradation of complex pollutants as well as the recyclability of catalysts. Besides, the novel “sandwich” structure could effectively regulate the band gap state and mobile route of carriers which could result in a more efficient separation and longer lifetimes of photo-excited electron-hole pairs. In addition, the kaolinite sheets could prevent TiO₂ nanoparticles aggregation and effectively control the grain size of nano TiO₂, and then the final composite has larger surface area and more reactive sites [25]. As shown in Fig. 5(b), the photocatalysis degradation follows the first-order kinetics. The kinetics can be expressed as follows: $\ln(C_0/C) = kt$. This equation presents the linear relationship between $\ln(C_0/C)$ and time, where C_0/C is the normalized as concentration variance of CIP, t is the reaction time, and k is the reaction rate constant (min⁻¹). It is observed that the rate constant of g-C₃N₄/TiO₂/kaolinite composite was calculated to be 0.00813 min⁻¹, which is about 5.35, 4.49 and 6.35 times higher than that of pure TiO₂, P25 and g-C₃N₄, respectively. Overall, it is believable that the construction of a heterojunction structure decorated on the

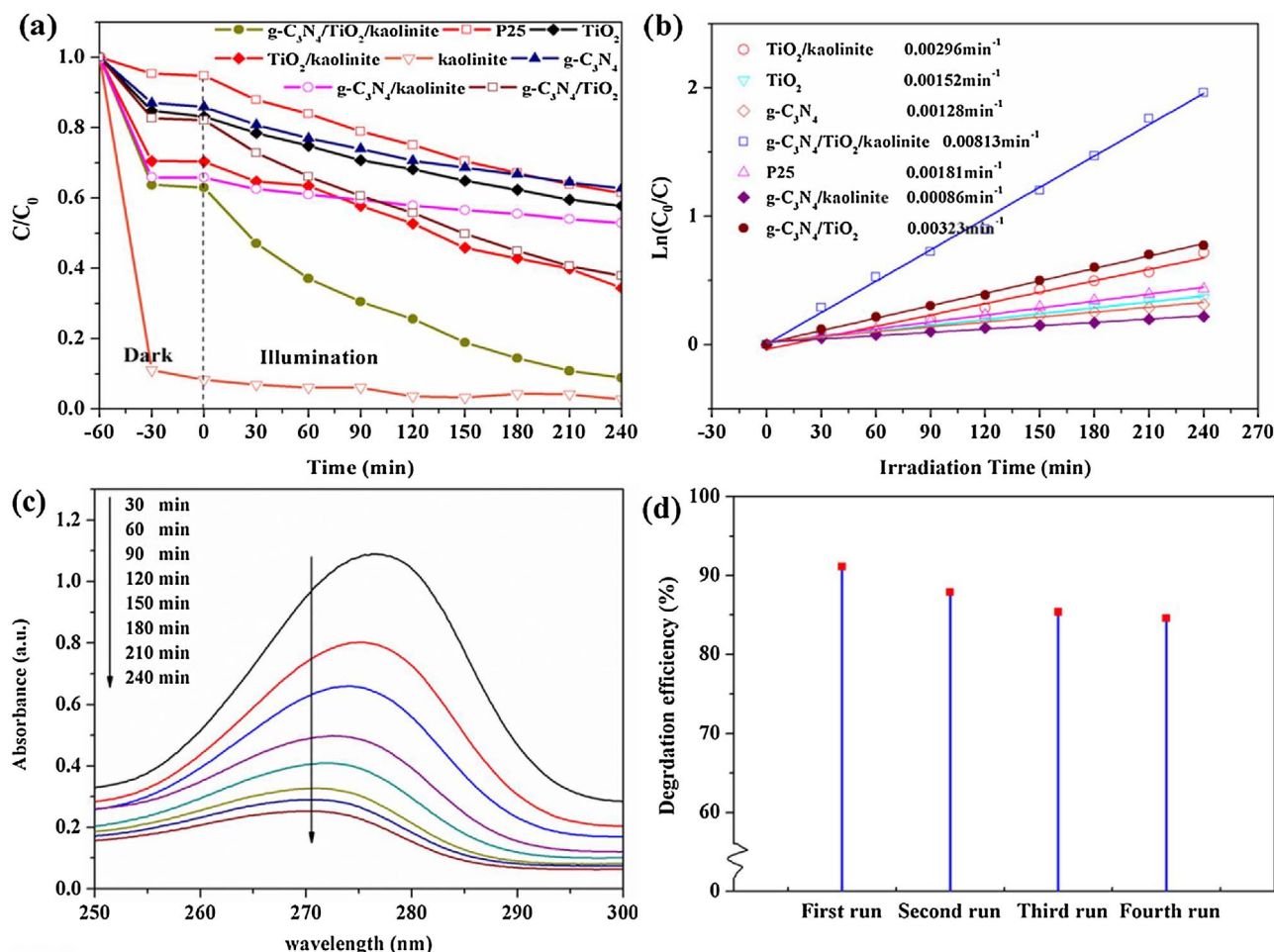


Fig. 5. (a) Photocatalytic degradation of CIP under visible light, (b) Linear transform $\ln(C_0/C)$ of the kinetic curves of CIP under visible light, (c) Absorption variance of CIP in liquid phase with time over the as-prepared $g-C_3N_4/TiO_2/kaolinite$ composite and (d) Reusability performance of $g-C_3N_4/TiO_2/kaolinite$ composite towards CIP.

layered kaolinite with enhanced visible light absorption ability and effective separation of carriers through chemical bond connection could effectively promote the photoactivities. The stability and reusability experiments were also conducted for the practical application of the synthesized composite. As shown in Fig. 5(d), it is noticed that the $g-C_3N_4/TiO_2/kaolinite$ composite still exhibited superb catalytic performance in the fourth cycle, demonstrating the recyclability and stable activity of the synthesized ternary “sandwich” structure. The comparison between initial and recycling XRD patterns of $g-C_3N_4/TiO_2/kaolinite$ composite as well as the HRTEM images of $g-C_3N_4/TiO_2/kaolinite$ composite after recycling were exhibited in Fig. S5 and Fig. S6, which could further demonstrate the structure stability of the $g-C_3N_4/TiO_2/kaolinite$ composite after recycling photocatalysis tests.

In this study, the degradation intermediates of CIP were detected by the LC/MS considering the incomplete mineralization. These by-products may result from the reaction at specific sites of CIP, such as the piperazine ring and the quinolone moieties [26]. A representative chromatogram after 120 min of irradiation as well as the corresponding mass spectra was shown in Fig. 6. Regarding the m/z ratios obtained in positive mode, intermediate structures of CIP were identified in the presence of the synthesized composite, and a possible mechanism of CIP photocatalytic degradation is proposed as illustrated in Fig. 7. First, the conversion of the amine function to amide was achieved [27]. Then the product P3 was obtained derived from the reductive dehalogenation, and in the later case, subsequent cleavage of carboxyl was observed which was corresponding to the product P2. Finally, further oxidation was conducted and the piperazine ring of CIP as well as partial quinolone moieties were completely destroyed (P1'). In another potential

pathway, amine side-chain oxidation (P1) was generated by loss of N atoms in the aniline and alkylamine structure [6]. Both routes would transform the CIP into small CO_2 and H_2O molecular with the continuous illumination. Besides, seen from Fig. 6, other relative high m/z ratios by-products were also detected. These intermediates could mainly be attributed to the secondary combination between the low m/z ratios by-products. For example, P5 was produced through establish the connection between the piperazine ring fragment and the CIP with the loss of a fluorine ion. P6 product with a retention time of 9.7 min was generated from the combination between the P1' and P3 products. P7 product was emerged from the link between P2 and P1 with the removal of fluorine ion. Furthermore, it is noticed that in each mass spectra, the detected dominant product was existed in two forms whose m/z ratios demonstrated a difference of 17, which could be ascribed to the increasing NH_4^+ in the aqueous system. This degradation process could be verified from the previous report as well [28].

S. aureus, a common waterborne microorganism, was chosen as the representative microorganism to evaluate the photocatalytic water disinfection performance of the synthesized composites. As displayed in Fig. 8, no obvious bacterial inactivation was observed in the dark control experiments for all the samples, indicating the non-toxicity of the photocatalysts as well as the references to the *S. aureus* cells during the test period. After 5 h visible light irradiation, it was found that almost no *S. aureus* was inactivated in the light control (visible light illumination without photocatalyst). The kaolinite displayed negligible disinfection efficiency as well. As for the $g-C_3N_4/TiO_2/kaolinite$ composite, the photocatalytic activity was obviously higher than the other references, demonstrating the beneficial effect of effective assembly

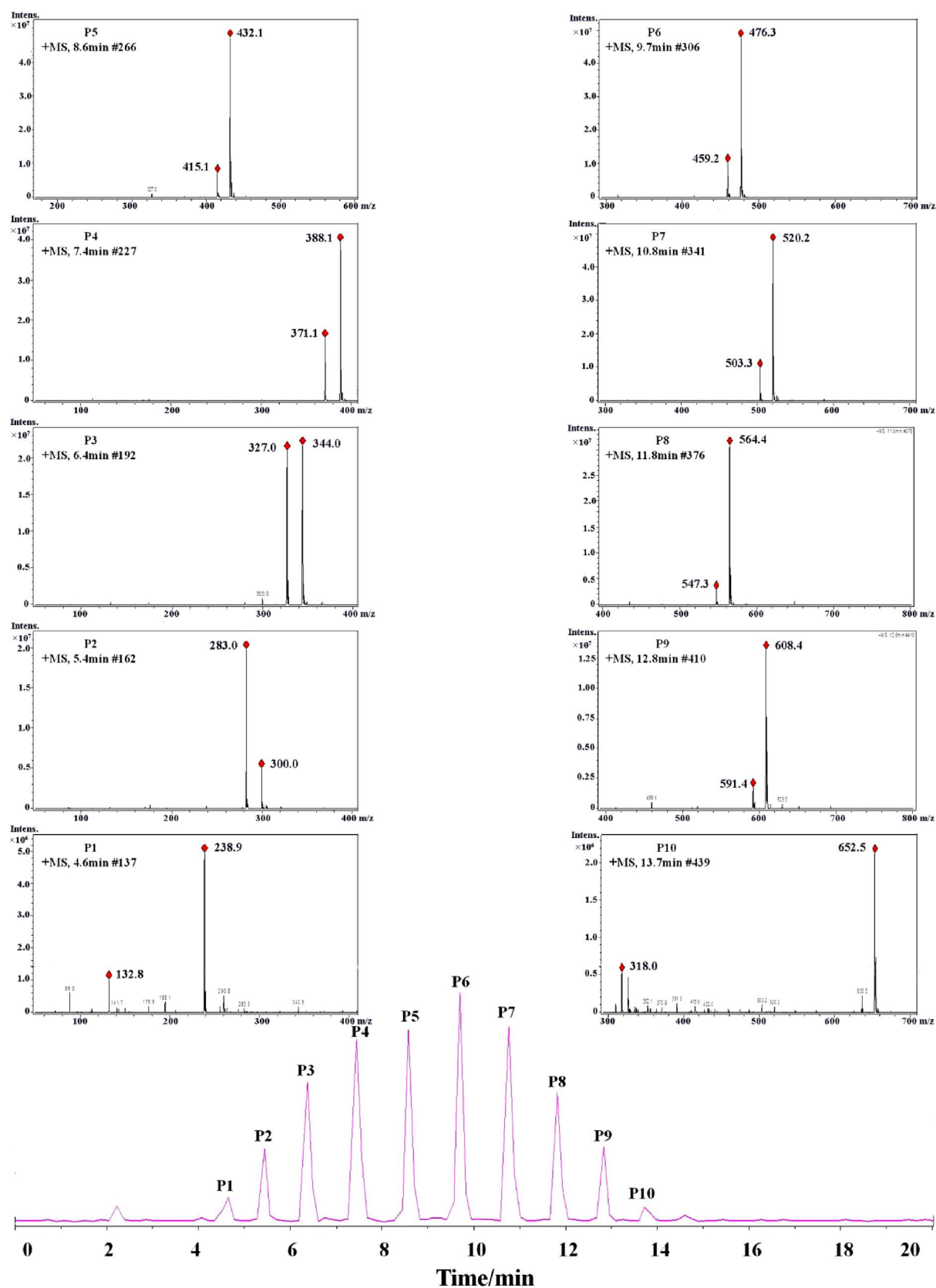


Fig. 6. Representative chromatogram of CIP and the corresponding mass spectra after 120 min of irradiation.

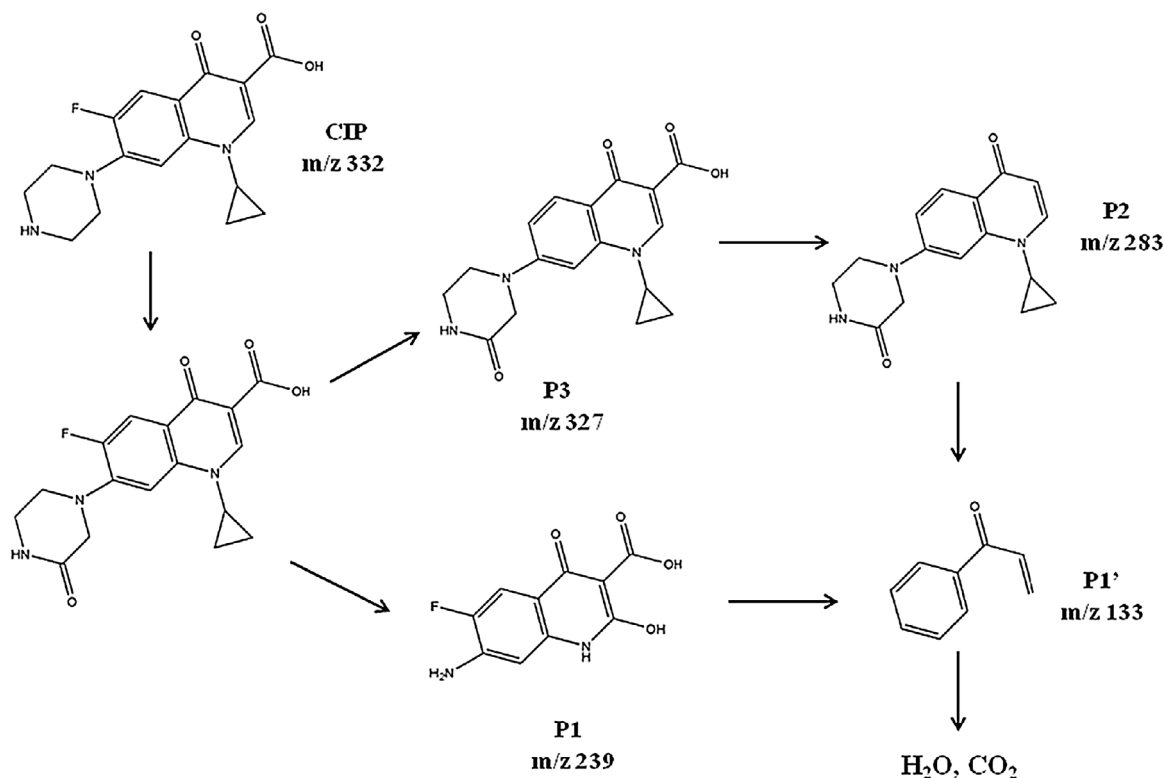


Fig. 7. Possible degradation pathways and byproducts of CIP in the presence of g-C₃N₄/TiO₂/kaolinite composite.

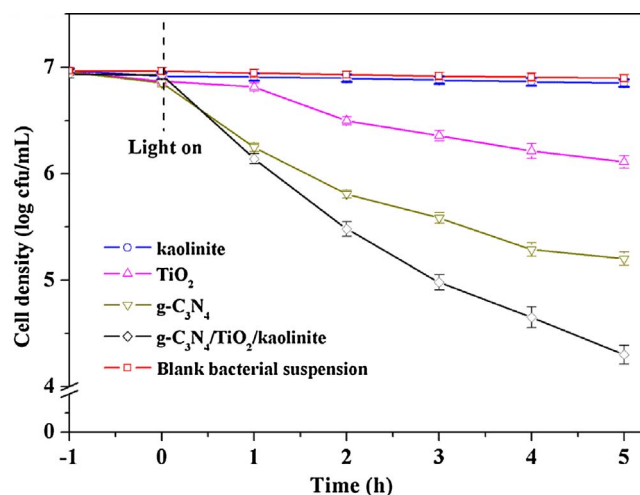


Fig. 8. Photocatalytic inactivation efficiency against *S. aureus* (around 1×10^7 cfu/mL, 60 mL) in the presence of the as-prepared samples.

between the natural layered kaolinite and the type II heterojunction formed by coupling TiO₂ with g-C₃N₄ [29].

In order to further investigate the active species in the degradation process, 10 mM of isopropanol (IPA), 1,4-benzoquinone (BQ), edentate disodium (EDTA-2Na) and silver nitrate (AgNO₃) were employed as the scavengers of hydroxyl radical ($\cdot\text{OH}$), superoxide radical ($\cdot\text{O}_2^-$), hole (h^+) and electron (e^-), respectively. Seen from Fig. 9(a), the degradation efficiency of CIP was slightly depressed after the addition of IPA and EDTA-2Na, indicating that only a few $\cdot\text{OH}$ and h^+ were in the presence during the degradation process. However, significant descend were observed when the BQ and AgNO₃ were added, suggesting the important roles of $\cdot\text{O}_2^-$ and e^- species in the photocatalytic process. This means the $\cdot\text{O}_2^-$ and e^- rather than $\cdot\text{OH}$ or h^+ play the dominant role in the decomposition process under visible light.

Photoluminescence spectra (PL) (Fig. 9(b)) were also conducted to demonstrate the charge separation efficiency of the synthesized composite. Weaker PL signal was observed in the presence of g-C₃N₄/TiO₂/kaolinite composite compared with pure g-C₃N₄, suggesting a lower recombination rate of the carriers [30]. Furthermore, the transient photocurrent responses and electrochemical impedance spectroscopy (EIS) of pristine samples as well as the synthesized composite were recorded in order to further understand the photogenerated charge separation and electron transfer performance (Fig. 9(c and d)). Notably, an enhanced photocurrent response and a smaller radius of the Nyquist circle were presented for the g-C₃N₄/TiO₂/kaolinite composite, which indicated that a greatly improved charge separation was obtained within the interfaces of the as-received composite [31,32].

Based on the aforementioned discussion and analyses, the photocatalytic mechanism for the 3D heterogeneous g-C₃N₄/TiO₂/kaolinite composite towards high-efficient degradation of CIP as well as strong bactericidal ability was tentatively proposed and schematically as illustrated in Scheme 2. For pure TiO₂ and g-C₃N₄, the photo-generated electrons and holes tend to recombine and only a fraction of them participated into the reaction process, which would result in a relative low activity [33]. For the synthesized heterogeneous g-C₃N₄/TiO₂/kaolinite composite, novel “sandwich” structure was established and chemically bonded interfacial contact was successfully achieved in this ternary system. Well dispersion of nano TiO₂ with smaller grain sizes on the surface of kaolinite and much more exposed g-C₃N₄ sheets assembled with TiO₂/kaolinite composite were realized as well. Generally, the performance of a photocatalyst is governed by two critical properties, namely the ability to utilize the solar spectrum and the efficacy of the generated electron-hole pairs for ROS (reactive oxygen species) production [34]. In this work, both the improvement of light harvesting and enhanced separation and transfer efficiency are the main factors for improving the photocatalytic performance. It is indicated that g-C₃N₄-TiO₂ Z-scheme photocatalytic system was established as exhibited in Scheme 2. According to previous reports, the CB and VB edge potentials of TiO₂ were at -0.24 eV and 2.96 eV, and the

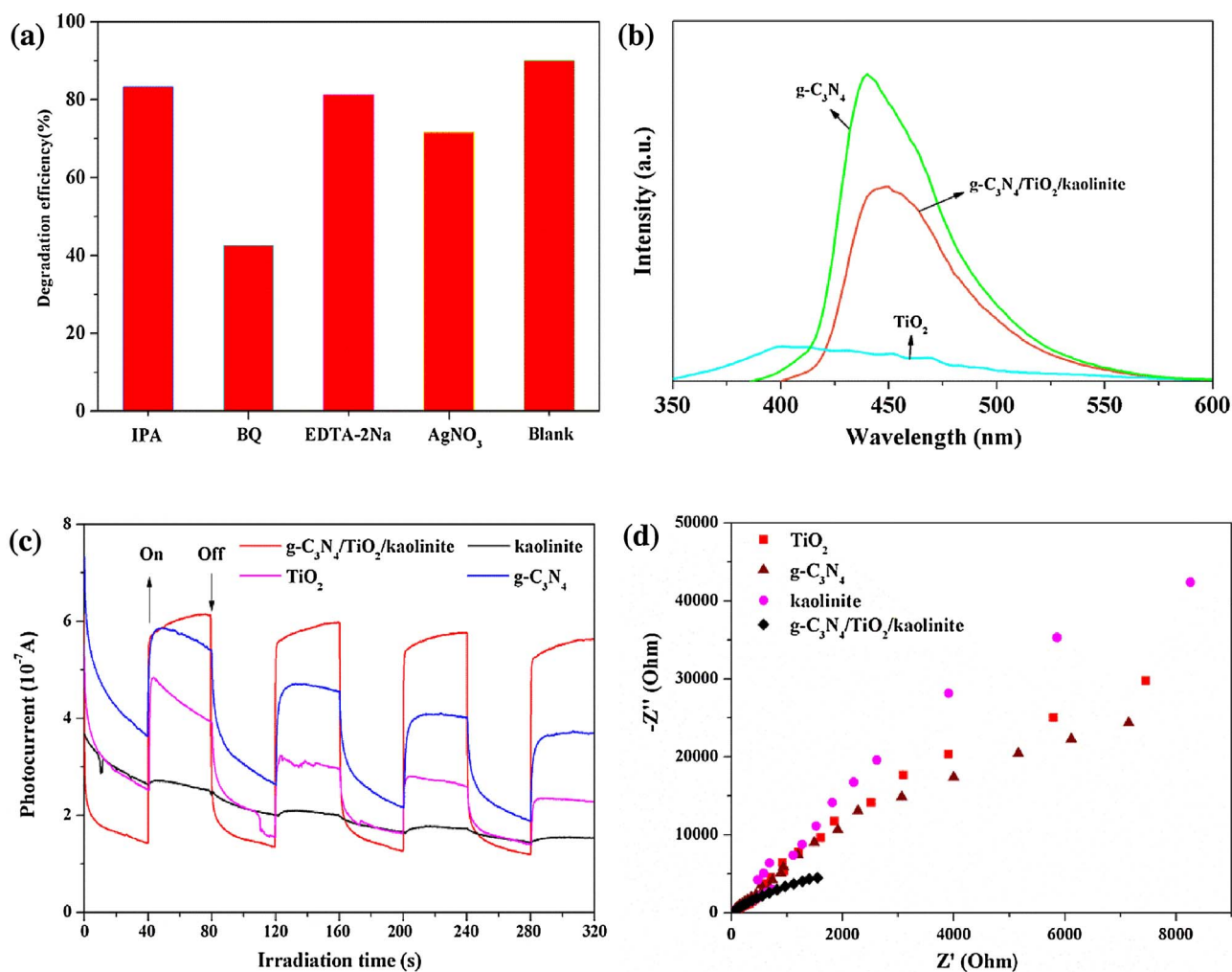
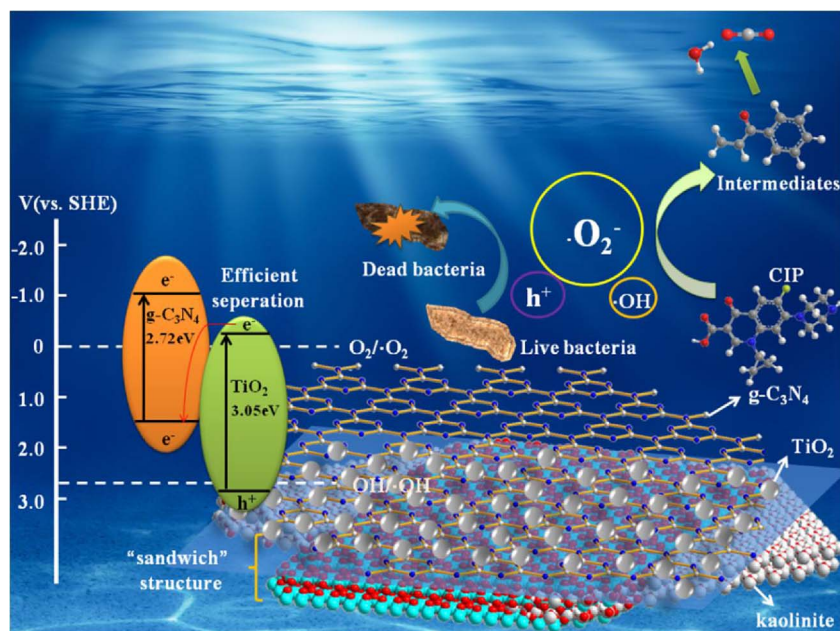


Fig. 9. (a) Trapping experiment of active species during the photocatalytic degradation of CIP over g-C₃N₄/TiO₂/kaolinite composite under visible light illumination, (b–d) PL spectra, Transient photocurrent and Nyquist plots of EIS for the as-prepared composite as well as the comparative samples.



Scheme 2. Schematic diagram of the enhancement mechanism for the degradation process under visible light towards g-C₃N₄/TiO₂/kaolinite composite.

corresponding CB and VB edge potentials of g-C₃N₄ were at -1.23 eV and 1.51 eV [35]. Under visible light illumination, the photo-induced holes tend to keep in the VB of TiO₂, while the electrons will transfer from the CB of TiO₂ to the VB of g-C₃N₄. Then the electrons in the VB of g-C₃N₄ are inclined to jump to its CB. This results in an efficient space separation of the photo-induced carriers. Besides, negative-charged kaolinite would be also beneficial for the separation of carriers due to the strong electrostatic repulsion [19]. Newly Ti–O–H bond would be formed in the preparation due to the rich hydroxyl on the kaolinite surface. This might further contributed to the highly efficient separation of carriers [36]. The photogenerated electrons in the CB of g-C₃N₄ could reduce the absorbed O₂ to produce $\cdot\text{O}_2^-$, which is due to the more negative position of CB of g-C₃N₄ than the O₂/ $\cdot\text{O}_2^-$ potentials. Moreover, the absorbed O₂ could also react with the water molecules and electrons to form H₂O₂. Finally, some generating H₂O₂ and $\cdot\text{O}_2^-$ could be transformed into hydroxyl radicals ($\cdot\text{OH}$) [12]. In this study, the main active specie ($\cdot\text{O}_2^-$) and the subordinate species ($\cdot\text{OH}$ and h^+) could effectively degrade the target pollutant (CIP) into small intermediates (piperazine ring, quinolone moieties, etc) and the ultimate products (CO₂ and H₂O). Bacteria (*S. aureus*) were also effectively degraded and wiped out by this process.

4. Conclusions

In conclusion, a novel 3D heterogeneous g-C₃N₄/TiO₂/kaolinite composite was fabricated via a mild sol-gel method associated with chemical stripping and self-assembly in this study. The morphological analysis and other characterizations confirmed the formation of the novel “sandwich” structure, in which a better dispersion of nano TiO₂ with smaller grain sizes, much more exposed g-C₃N₄ sheets, enlarged surface area as well as enhanced visible-light absorption ability were achieved. The as-synthesized g-C₃N₄/TiO₂/kaolinite composite exhibited enhanced photocatalytic activity in degrading CIP under visible-light illumination, the apparent rate constant of which is almost 5.35 times, 6.35 times and 4.49 times that of pure TiO₂, g-C₃N₄ and P25, respectively. Good reusability of the g-C₃N₄/TiO₂/kaolinite composite demonstrated the recyclability and stable activity of the synthesized ternary structure. Furthermore, the as-received composite also exhibits higher disinfection ability towards *S. aureus* compared with the other references. Based on scavengers experiments, PL and EIS analysis, the superoxide radical ($\cdot\text{O}_2^-$) is proved to be the main active species in the degradation process, and the enhancement of the photocatalytic performance should be attributed to both the improvement of light harvesting and the enhanced separation and transfer efficiency. The present study provides new insight into the construction of highly efficient visible-light driven 3D composite photocatalysts, which exhibit promising application prospect in the fields of the organic pollutants degradation and bacteria inactivation.

Acknowledgements

The authors gratefully acknowledge the financial support provided by the National Natural Science Foundation of China (Grant No. 51504263) and the Fundamental Research Funds for the Central

Universities (2015QH01).

Appendix A. Supplementary data

Supplementary data associated with this article can be found, in the online version, at <http://dx.doi.org/10.1016/j.apcatb.2017.08.044>.

References

- [1] Y. Li, C. Zhang, D. Shuai, S. Naraginti, D. Wang, W. Zhang, Water Res. 106 (2016) 249–258.
- [2] W. Bing, Z. Chen, H. Sun, P. Shi, N. Gao, J. Ren, X. Qu, Nano Res. 8 (2015) 1648–1658.
- [3] A. Hassani, A. Khataee, S. Karaca, J. Mol. Catal. A Chem. 409 (2015) 149–161.
- [4] S. Bae, D. Kim, W. Lee, Appl. Catal. B Environ. 134–135 (2013) 93–102.
- [5] J. Huang, W. Ho, X. Wang, Chem. Commun. 50 (2014) 4338–4340.
- [6] X.X. Zhang, R. Li, M. Jia, S. Wang, Y. Huang, C. Chen, Chem. Eng. J. 274 (2015) 290–297.
- [7] M.J. Muñoz-Batista, O. Fontelles-Carceller, M. Ferrer, M. Fernández-García, A. Kubacka, Appl. Catal. B Environ. 183 (2016) 86–95.
- [8] S.D. Perera, R.G. Mariano, K. Vu, N. Nour, O. Seitz, Y. Chabal, K.J. Balkus Jr., ACS Catal. 2 (2012) 949–956.
- [9] Z. Tong, D. Yang, T. Xiao, Y. Tian, Z. Jiang, Chem. Eng. J. 260 (2015) 117–125.
- [10] L. Sun, X. Zhao, C.J. Jia, Y. Zhou, X. Cheng, P. Li, L. Liu, W. Fan, J. Mater. Chem. 22 (2012) 23428–23438.
- [11] C. Li, Z. Sun, Y. Xue, G. Yao, S. Zheng, Adv. Powder Technol. 27 (2016) 330–337.
- [12] F. Chen, Q. Yang, Y. Wang, J. Zhao, D. Wang, X. Li, Z. Guo, H. Wang, Y. Deng, C. Niu, Appl. Catal. B Environ. 205 (2016) 133–147.
- [13] G.K. Zhang, X.M. Ding, F.S. He, X.Y. Yu, J. Zhou, Y.J. Hu, J.W. Xie, Langmuir ACS J. Surf. Colloids 24 (2008) 1026–1030.
- [14] D. Shao, X. Wang, Q. Fan, Microporous Mesoporous Mater. 117 (2009) 243–248.
- [15] J. Ma, D. Huang, W. Zhang, J. Zou, Y. Kong, J. Zhu, S. Komarneni, Chemosphere 162 (2016) 269–276.
- [16] Z. Sun, C. Bai, S. Zheng, X. Yang, R.L. Frost, Appl. Catal. A: Gen. 458 (2013) 103–110.
- [17] B. Dou, V. Dupont, W. Pan, B. Chen, Chem. Eng. J. 166 (2011) 631–638.
- [18] C. Li, Z. Sun, W. Huang, S. Zheng, J. Taiwan Inst. Chem. Eng. 66 (2016) 363–371.
- [19] Z. Sun, G. Yao, X. Zhang, S. Zheng, R.L. Frost, Appl. Clay Sci. 129 (2016) 7–14.
- [20] L. Ma, H. Fan, K. Fu, Y. Zhao, Chemistryselect 1 (2016) 3730–3738.
- [21] C. Li, Z. Sun, X. Li, L. Liu, S. Zheng, Adv. Powder Technol. 27 (2016) 2051–2060.
- [22] C. Li, Z. Sun, L. Liu, W. Huang, S. Zheng, RSC Adv. 6 (2016) 91002–91011.
- [23] K. Peng, L. Fu, J. Ouyang, H. Yang, Adv. Funct. Mater. 26 (2016) 2666–2675.
- [24] Y. Cui, Q. Ma, X. Deng, Q. Meng, X. Cheng, M. Xie, X. Li, Q. Cheng, H. Liu, Appl. Catal. B Environ. 206 (2017) 136–145.
- [25] J. Zhou, M. Zhang, Y. Zhu, Phys. Chem. Chem. Phys. 17 (2015) 3647–3652.
- [26] A.R. Silva, P.M. Martins, S. Teixeira, S.A.C. Carabineiro, K. Kuehn, G. Cuniberti, M.M. Alves, S. Lancerosmendez, L. Pereira, RSC Adv. 1 (2016) 1–20.
- [27] M. Sturini, A. Speltini, F. Maraschi, A. Profumo, L. Pretali, E.A. Irastorza, E. Fasani, A. Albini, Appl. Catal. B Environ. 119–120 (2012) 32–39.
- [28] T. Paul, M.C. Dodd, T.J. Strathmann, Water Res. 44 (2010) 3121–3132.
- [29] W. Wang, J.C. Yu, D. Xia, P.K. Wong, Y. Li, Environ. Sci. Technol. 47 (2013) 8724–8732.
- [30] L. Ma, H. Fan, J. Wang, Y. Zhao, H. Tian, G. Dong, Appl. Catal. B Environ. 190 (2016) 93–102.
- [31] S. Zhang, J. Li, X. Wang, Y. Huang, M. Zeng, J. Xu, J. Mater. Chem. A 3 (2015) 10119–10126.
- [32] L. Ma, H. Fan, M. Li, H. Tian, J. Fang, G. Dong, J. Mater. Chem. A 3 (2015) 22404–22412.
- [33] J. Yu, S. Wang, J. Low, W. Xiao, Phys. Chem. Chem. Phys.: PCCP 15 (2013) 16883–16890.
- [34] C. Liu, D. Kong, P.C. Hsu, H. Yuan, H.W. Lee, Y. Liu, H. Wang, S. Wang, K. Yan, D. Lin, Nat. Nanotechnol. 11 (2016) 1098–1104.
- [35] G. Li, X. Nie, J. Chen, Q. Jiang, T. An, P.K. Wong, H. Zhang, H. Zhao, H. Yamashita, Water Res. 86 (2015) 17–24.
- [36] K.K. Mamulová, J. Tokarský, P. Kovář, S. Vojtěšková, A. Kovářová, B. Smetana, J. Kukutschová, Č.P.V. Matějka, J. Hazard. Mater. 188 (2011) 212–220.